

# An Accessible Planar Ion Trap for Experiential Learning in Quantum Technologies

Robert E. Thomas,<sup>1,2</sup> Cole E. Wolfram,<sup>1</sup> Noah B. Warren,<sup>1</sup>  
Isaac J. Fouch,<sup>1</sup> Boris B. Blinov,<sup>1</sup> and Maxwell F. Parsons<sup>2,\*</sup>

<sup>1</sup>*Department of Physics, University of Washington,  
Seattle, Washington 98195, United States of America*

<sup>2</sup>*Department of Electrical & Computer Engineering, University of Washington,  
Seattle, Washington 98195, United States of America*

## Abstract

We describe an inexpensive and accessible instructional setup which explores ion trapping with a planar linear ion trap. The planar trap is constructed using standard printed circuit board manufacturing and is designed to trap macroscopic charged particles in air. Trapping, shuttling, and splitting is demonstrated to students using these particles, visible to the naked eye. Students have control over trap voltages and can compare properties of particle motion to an analytic model of the trap using a computer vision program for particle tracking. Learning outcomes include understanding the design considerations for planar RF traps, mechanisms underpinning ion ejection, the physics of micromotion, and methods of data analysis using standard computer vision libraries.

## I. INTRODUCTION

In recent years, rapid progress in controlling quantum states and entanglement between particles has paved the way for advancements in quantum computation, communication, and sensing. This “second quantum revolution” is transitioning quantum science from academic research into industry-scale efforts, necessitating a corresponding expansion in quantum workforce development.<sup>1</sup> To develop future quantum technologies, we should bridge the gap between engineering and physics by exposing engineers to quantum-specific expertise and training physicists in engineering practices. A key component of this training is providing students with hands-on access to quantum hardware, enabling them to apply classroom concepts in practical settings.

Trapped atomic ions are among the most effective qubit platforms for controlling and using quantum entanglement, demonstrating record entanglement fidelities and qubit connectivity.<sup>2-4</sup> Typically, ions are confined to a one-dimensional (1D) trapping region.<sup>4</sup> As more ions are added to a 1D trap, challenges arise, such as motional-mode crowding that hampers two-qubit gate fidelity and speeds.<sup>4-7</sup> One solution to these issues is the use of quantum charge-coupled devices (QCCDs).<sup>8</sup> In a QCCD, ions are trapped using radiofrequency (RF) electric fields.<sup>4,8</sup> Ions can be broken into short chains and those chains can be split, merged, and shuttled using segmented DC electrodes.<sup>4,6,8</sup> This approach enables the movement of pre-loaded ions from a loading region to an interaction region, where high-fidelity gate operations are performed on a small group of ions, as well as to designated memory locations.<sup>6,8</sup> Using these systems for training purposes is challenging due to the integration of ultra-high vacuum systems, microfabricated traps, high-power RF signals, and complex laser systems for cooling, qubit manipulation, and readout. By focusing on the physics and engineering of the trap itself, we can reduce this complexity and create an accessible instructional laboratory setup.

In this paper, we present an inexpensive, easily fabricated 5-rail planar ion trap for use in physics and engineering laboratory courses to explore the basic functionalities needed for the QCCD architecture. Our trap is designed on a standard printed circuit board (PCB) to trap charged lycopodium moss spores in air using a combination of static and 60 Hz oscillating electric fields. To maintain consistency with atomic ion traps, we refer to the charged lycopodium spores as “ions” and the 60 Hz fields as “RF” throughout this paper. With

this setup, students can explore the fundamental principles of trapping charged particles, understand design considerations for planar ion traps (such as the impact of trap properties and charge-to-mass ratio on stability), examine the origin of micromotion and how to compensate for it, and demonstrate ion shuttling and splitting between trapping regions. This setup was initially designed and built by undergraduate physics and electrical engineering students as an independent project.

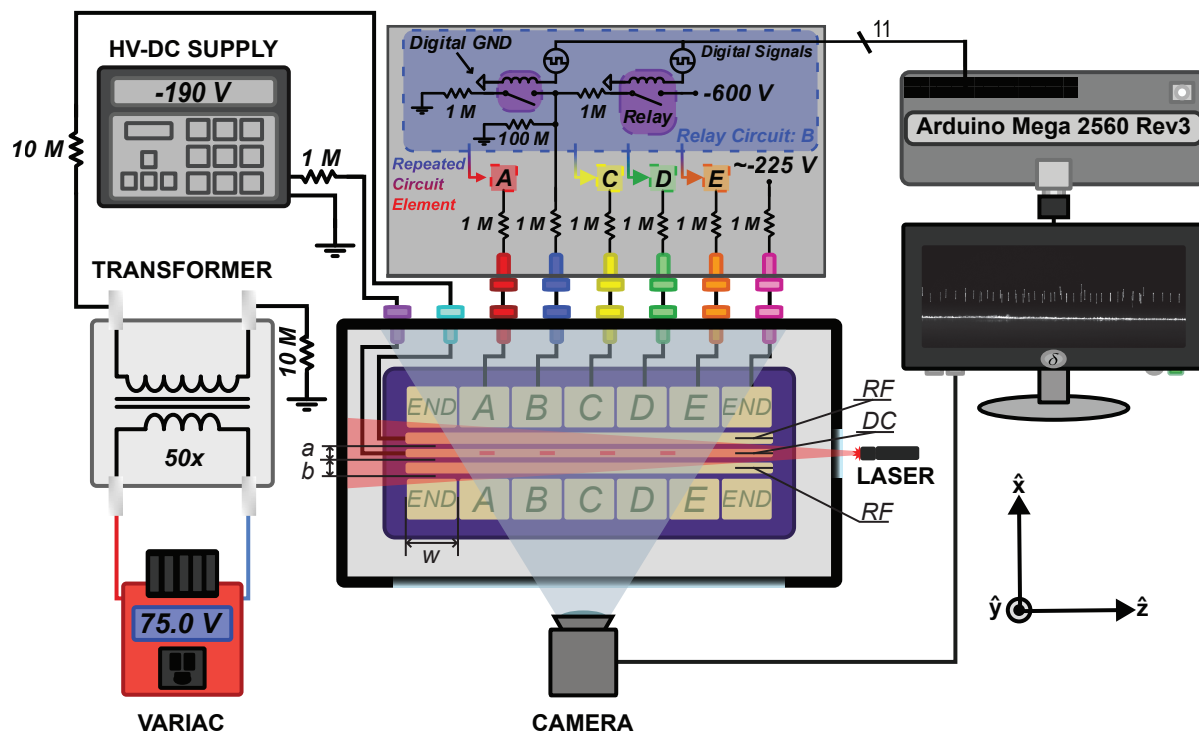


FIG. 1: The primary components of the apparatus are a variac, step-up transformer, high voltage supply, enclosure, camera, computer, relay circuit for controlling the segmented electrodes, Arduino, and planar trap. We show the main circuit elements involved in controlling the segmented electrodes for ion shuttling. The variac ranges from 0 V to 120 V peak-to-peak at 60 Hz with a corresponding output range of 0 kV to 6 kV peak-to-peak from the transformer. One leg of the transformer is grounded along with the other high voltage supplies. The HV-DC supply typically runs from 0V to  $-250$  V. Two digital signal lines from the Arduino control the voltage on each of the 5 pairs of shuttling electrodes while the digital ground is shared between all the signal lines. The endcap electrodes are separately controlled with a high voltage DC-DC converter providing a maximum voltage of approximately  $-225$  V.

## II. DESCRIPTION OF SETUP

We developed a planar ion trap for macroscopic particles at atmospheric pressure which accepts user inputs to control ion confinement, shuttling and splitting. This trap, shown in Fig. 1, is manufactured on a standard PCB and consists of five rails, with segmented outer electrodes that control in-trap shuttling. We use high voltage reed relays actuated via an Arduino microcontroller to configure a set of voltage dividers that provide each shuttling electrode with one of three programmable voltages. In addition to the trap and relay circuits, our setup features a 3D printed enclosure for user safety and turbulence reduction, an illumination laser, and a camera for imaging. Video data is processed with the OpenCV python package. We provide all relevant files, including image processing code, CAD models, Gerber files, and code to generate the figures in this paper in an associated GitHub repository.<sup>9</sup>

**Charged Particles (“Ions”):** We trap charged lycopodium moss spores which have a radius of approximately 26 microns and are visible to the naked eye with adequate illumination.<sup>10,11</sup> They are charged with a Teflon wand and a wool cloth through the triboelectric effect<sup>10,11</sup> to a charge-to-mass ratio ranging from  $2 \times 10^{-4}$  C/kg to  $5 \times 10^{-2}$  C/kg.<sup>10,12</sup> The Teflon rod serves the dual purpose of charging the ions while shielding the user from the high voltages of the planar trap’s electrodes.<sup>10</sup> Similar macroscopic traps have used polyethylene microspheres, borosilicate glass, stainless steel spheres, aluminum spheres, aluminum oxide spheres, anthracene dust particles, glycerin oil droplets, borate particles, sodium particles, carbonate particles, and lucite particles.<sup>10,13–16</sup> Lycopodium moss spores because they are cheap, monodispersed, roughly spherical, non-toxic, easily chargeable with the method described above, and are non-conductive to prevent arcing between electrodes due to accumulation of ions on the planar trap’s surface.<sup>11</sup>

**Planar Trap Geometry:** Our electrode geometry is a 5-rail planar trap, in part due to its popularity in industry because of its compatibility with standard microfabrication techniques.<sup>4,8,17,18</sup> The geometry consists of a central DC electrode of dimensions 139.6 mm by 3.2 mm, two high voltage RF electrodes of dimensions 139.6 mm by 4.2 mm, and two complementary rails of seven segmented DC electrodes of dimensions 18.9 mm by 15.5 mm whose voltages are independently controllable. The dielectric separation between the DC and high voltage RF is 2.0 mm, the separation between the RF and segmented electrodes

is 2.0 mm, and the separation between segmented electrodes is 1.0 mm. Every electrode has 1.0 mm radius fillets to prevent arcing due to the high electric fields produced at sharp electrode corners.<sup>19</sup> The two RF electrodes are connected and each segmented electrode on the top row of the trap is directly connected to the correspondingly labeled segmented electrode on the bottom row, labeled *A*, *B*, *C*, *D*, or *E*. The four corner endcap electrodes are also shorted together. We manufactured these electrodes onto a two layer PCB which has FR408HR as an insulator with a dielectric strength of 70 kV/mm.

**Circuits:** The RF electrode voltage is provided by a variac connected to a step-up transformer to raise the voltage from 0 – 120 V to 0 – 6 kV peak-to-peak at 60 Hz. One leg of the transformer is treated as the high voltage ground. This reference is shared among the other high voltage supplies including a high voltage DC-DC converter which supplies the high voltages on the endcap electrodes. The other leg is connected to the two high-voltage RF electrodes. A 10 M $\Omega$  resistor on each transformer leg limits the current in case of a short.<sup>10,11</sup> The segmented electrode driver circuit is supplied a –600 V input voltage which is fed into a voltage divider, reducing the voltage to approximately –490 V (high), –260 V (low), and –10 V (off) depending on the configuration of the high voltage reed relays. We have measured the switching time of the divider circuits to be approximately 4.2 ms. The exact output relative to the idealized circuit described in Fig. 1 is limited by the 5% tolerance of our chosen resistors. Each output has a corresponding 1 M $\Omega$  resistor before connecting to each segmented electrode pair to limit the current on the electrodes in the case of a short. The DC electrode has an applied voltage within the range of approximately 0 V to –250 V which is sourced from a Stanford Research Systems Model PS350 high voltage DC power supply.

The planar trap is housed in an enclosure made out of polylactic acid (PLA) with acrylic optical ports on two perpendicular faces of the enclosure to allow for illumination and imaging of the ions. The enclosure secures the planar trap in place, reduces air turbulence, houses the high voltage wires, and provides a physical barrier between the user and the high voltage electrodes. It was designed to be printed on a 3D printer with a print volume of 255 mm by 155 mm by 170 mm.

**Imaging and Image Processing:** We use a 1 mW laser to illuminate the ions and image the scattered light with a FLIR Blackfly S monochrome camera which has a maximum frame rate of 60 frames per second and resolution of 1,616 by 1,240 pixels. For the experiments

described here, we used a 6 mm focal length lens with an aperture of  $f/1.85$  and a 25 mm focal length lens with an aperture of  $f/1.4$ . To automate data analysis, we use blob detection methods from OpenCV to track the motion of the trapped ions from video files.<sup>20</sup> This method incorporates a thresholding algorithm followed by filtration of resulting connected regions by size to isolate trapped ions from background noise in the image.

### III. ANALYTIC MODEL

Students can compare experimental properties of the 5-rail trap with an analytic model developed by M.G. House.<sup>21</sup> The analytic model of the 5-rail planar trap has a central ground electrode of length  $a$ , two RF electrodes of lengths  $b$ , and segmented electrodes of widths  $w$ .<sup>21</sup> The model assumes that the widths of the central and RF electrodes extend out infinitely, the lengths of the segmented electrodes extend out infinitely in the direction pointing out of the trapping region along the  $x$ -axis, each electrode is rectangular, the electrodes have constant voltage on their surface, and the potential goes to zero as you approach infinity in the direction normal to the trap surface.<sup>21</sup> Dielectric material between electrodes is necessary to prevent arcing and dielectric breakdown between neighboring electrodes. To account for the potential at the dielectric, we incorporated a linear interpolation between the voltages on the electrodes on either side of a dielectric gap.<sup>21</sup> We compared this interpolation to ignoring the gaps by assuming the electrodes extend into the dielectric region and found slightly better experimental agreement in ion height versus DC electrode voltage. Following House, the definitions for  $a$ ,  $b$  and  $w$  are the dimensions of the central, RF, and outer segmented electrodes respectively from the center of one dielectric gap to the other. We chose the widths of the segmented electrodes to be identical, based upon recommendation from Nizamani and Hensinger.<sup>22</sup>

Earnshaw's theorem prohibits electrostatic fields from confining a charged particle. To circumvent this, ion traps use a combination of DC ( $\phi_{\text{DC}}$ ) and RF ( $\phi_{\text{RF}}$ ) potentials for confinement.<sup>21,23</sup> At a given moment in time  $t$ , the potential in free space ( $\phi$ ) at position  $\mathbf{r}$  can be written as

$$\phi(\mathbf{r}, t) = \phi_{\text{DC}}(\mathbf{r}) + \phi_{\text{RF}}(\mathbf{r}) \cos \Omega t \quad (1)$$

for some angular frequency  $\Omega$ .<sup>21,23</sup> With the correct balance of applied DC and RF voltages, electrode dimensions, and angular frequency  $\Omega$ , one can confine an ion in the trap via the

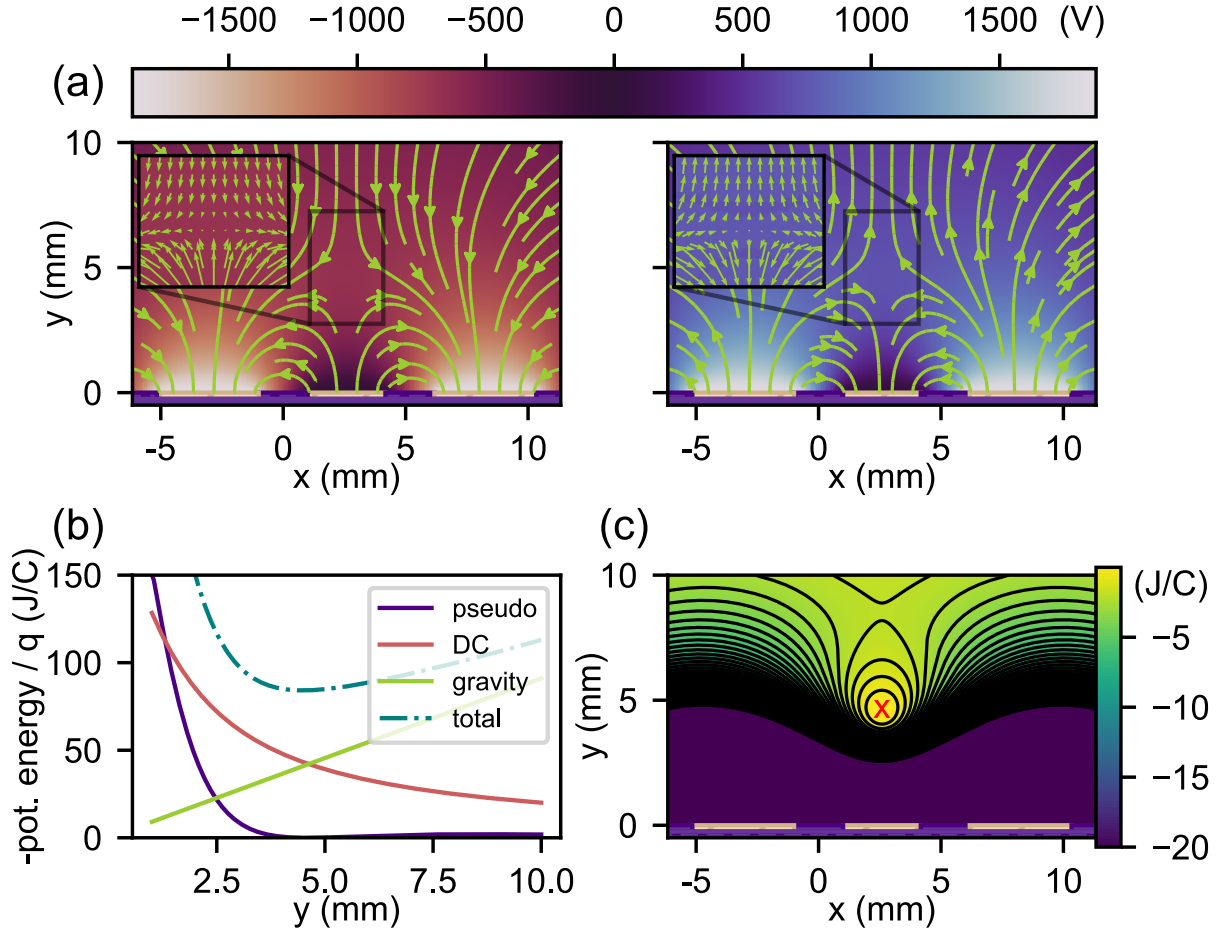


FIG. 2: Model of the planar trap potentials. Panel (a) shows the electric potential with field lines plotted at two instances of the RF potential that are  $\pi$  radians out of phase. The RF electrode voltages are at their minimum (left) and maximum (right). Panel (b) shows a y-cut of the potential energy normalized by the charge with a breakdown of contributions to the trapping potential when the DC electrode voltage is at 209 V. This voltage corresponds to alignment of the particle height with the RF null for a particle with charge-to-mass ratio of 1.08 J/C. Panel (c) shows only the pseudopotential energy from the RF electrodes, normalized by the charge, with the RF null labeled by the red ‘x’.

average forces on the ion over an RF cycle. This method of confinement creates two characteristic forms of motion for the ions: micromotion, which has a relatively small amplitude of oscillation at a frequency of the rotating RF field,  $\Omega$ , and secular motion, which corresponds to motion of the particle in the time-averaged trapping potential and has frequencies typically much lower than micromotion corresponding to the resonances of the trap.<sup>24</sup> One can approximately determine the trapped ion’s potential energy in terms of only its secular motion via the pseudopotential approximation, which averages the rotating field over time

to give a time-independent potential energy function

$$\psi(\mathbf{r}) = \frac{q^2}{4m\Omega^2} |\nabla\phi_{\text{RF}}(\mathbf{r})|^2 \quad (2)$$

where  $q$  is the charge of the ion and  $m$  is the mass of the ion.<sup>21</sup>

The electric field from the RF electrodes at times  $t = 0$  and  $t = \frac{\pi}{\Omega}$  is shown in Fig. 2a. From the insets, one can see that the instantaneous field configurations can only stabilize a charged particle along one dimension at a time. When time-averaging the forces according to the pseudopotential approximation, a clear potential minimum appears, as shown in Fig. 2c. With the addition of the gravitational potential ( $\phi_{\text{G}}$ ) due to the earth and the potential from the DC electrode ( $\phi_{\text{DC}}$ ), one can approximate the total time-independent potential energy function of an ion in the trap, normalized by the charge, as  $\mathcal{U}(x, y)/q =$

$$\frac{1}{\gamma}\phi_{\text{G}}(x, y) + \phi_{\text{DC}}(x, y) + \frac{\gamma}{4\Omega^2} |\nabla\phi_{\text{RF}}(x, y)|^2 \quad (3)$$

where  $\gamma$  is defined to be the charge-to-mass ratio  $q/m$  and  $\mathcal{U}$  is independent of  $z$  due to translational symmetry of the model along the  $z$ -axis when all segmented electrodes are grounded. The specific functional forms of  $\phi_{\text{RF}}$  and  $\phi_{\text{DC}}$  can be determined via the geometry of the analytic model as described in the appendix. A graph of the individual potential energy functions in units of joules per coulomb in addition to their sum along the unit normal of the central electrode,  $\hat{y}$  at  $x = a/2$ , is shown in Fig. 2b. As one moves in the  $\hat{y}$  direction at  $x = a/2$ , the pseudopotential for the 5-rail planar trap geometry will have a shape where there is a local minimum followed by a local maximum followed by an asymptotic approach to 0 V. The local minimum of the pseudopotential is called the RF null, where the ion experiences no net force. The ion height within the trap is determined by the overall potential minimum, including gravity and the DC electrode, with individual contributions shown in Fig. 2b.



## IV. LABORATORY EXERCISES

### A. Measuring charge-to-mass ratio and exploring motion of a single trapped ion

The charge-to-mass ratio ( $\gamma$ ) of an ion in an ion trap is an important quantity for trapped ion stability. Students can explore two methods of determining  $\gamma$ , using an applied negative voltage on the central DC electrode.

**Method 1, Fitting  $\gamma$  to height vs. DC electrode voltage data:** For ion confinement above the trap, the particle must be at a local minimum of  $\mathcal{U}$ . At the local minimum,  $\mathbf{r}_{\min} \equiv (a/2, y_{\min})$  for some  $y_{\min} > 0$ . Therefore  $-\nabla\mathcal{U}(\mathbf{r})\big|_{\mathbf{r}_{\min}} = \mathbf{0}$ . Visually inspecting the total potential in Fig. 2 panel (b) suggests that there exists a unique minimum  $y_{\min}$  for  $y > 0$ . Thus,  $y_{\min} =$

$$\operatorname{argmin}_{y>0} \left\{ \frac{1}{\gamma} \phi_G\left(\frac{a}{2}, y\right) + \phi_{\text{DC}}\left(\frac{a}{2}, y\right) + \frac{\gamma}{4\Omega^2} |\nabla\phi_{\text{RF}}\left(\frac{a}{2}, y\right)|^2 \right\}.$$

One can determine  $\gamma$  experimentally by measuring ion height values with different applied DC voltages and fitting that data to corresponding  $y_{\min}$  points from the analytic model at the same applied DC voltages. This method is shown in Fig. 4a.

**Method 2, determining  $\gamma$  from minimal micromotion amplitude:** The micromotion amplitude ( $\alpha$ ), to first order, is related to the displacement from the RF null by  $\alpha \propto |y_{\text{null}} - y|$ .<sup>25</sup> Therefore, one can experimentally determine the RF null position from the stationary height of the ion above the trap where the micromotion is minimized. We will consider an ion that is stably trapped at the RF null,  $\mathbf{r}_{\text{null}} = (a/2, y_{\text{null}})$ . The force on an ion is given by the negative gradient of  $\mathcal{U}(x, y)$ . Therefore,  $-\nabla\mathcal{U}(x, y) = -m\nabla\phi_G(x, y) - q\nabla\phi_{\text{DC}}(x, y) - (q^2/4m\Omega^2)\nabla(|\nabla\phi_{\text{RF}}(x, y)|^2)$ , and a stably trapped ion implies that  $-\nabla\mathcal{U}(x, y)\big|_{\mathbf{r}_{\text{null}}} = \mathbf{0}$ . Since the RF null location is defined as a local minimum of the RF pseudopotential,  $(q^2/4m\Omega^2)\nabla(|\nabla\phi_{\text{RF}}(x, y)|^2)\big|_{\mathbf{r}_{\text{null}}} = \mathbf{0}$ . Therefore, when an ion sits at the RF null, the vertical force from the DC electrodes balances gravity, i.e.

$$\begin{aligned}
(-m\nabla(gy) - q\nabla\phi_{\text{DC}}(x, y))\Big|_{\mathbf{r}_{\text{null}}} &= \mathbf{0} \\
\implies \gamma = \frac{q}{m} &= \frac{-g}{|\nabla\phi_{\text{DC}}(\mathbf{r}_{\text{null}})|}.
\end{aligned}
\tag{4}$$

$y_{\text{min}}$ , like in method 1, is the location of the total potential energy function’s minimum (normalized by charge), which will experimentally be the location of the centroid of oscillation of the ion’s micromotion in the trap. By minimizing micromotion, one experimentally determines when  $y_{\text{min}} \approx y_{\text{null}}$  since  $\alpha \propto |y_{\text{null}} - y|$ , which, with Eq. 4, allows for one to calculate  $\nabla\phi_{\text{DC}}$  at  $\mathbf{r}_{\text{null}} = (a/2, y_{\text{null}})$  and thus determine  $\gamma$ . This method is demonstrated in Fig. 4a.

**Experimental Methods:** We image the ions with a 25 mm focal length lens and calibrate the distance per pixel units in the video by imaging a fine ruler vertically above the DC electrode. For loading ions into the trap, the shuttling electrodes  $A$ - $E$  are set to low, the variac is set to 75 V, and the endcap electrodes are set to  $-150$  V DC. We charge and deposit an ensemble of ions into the trapping region by flicking the Teflon rod that has been dipped in lycopodium spores above the trap through a hole in the enclosure. To isolate a single ion, we lower the AC trapping voltage slowly until only a single ion remains in the trap, effectively filtering out the ions with lower charge-to-mass ratios. Then, the variac is returned to 75 V. The motion of the ion is captured in a video. The video collection begins with an initial central electrode voltage of  $-40$  V, which we then decrease by  $-5$  V every 5 seconds until the ion is ejected from the trap.

The data analysis code uses OpenCV to identify the location and dimension of the ion’s motion throughout the video, as shown in Fig. 3a. Increasing the exposure time of the camera causes the illumination of the ion’s complete trajectory, which appears as a “streak” in the video and allows for measurement of micromotion amplitude. We operate the camera at fixed frame rate and determine time from the frame number. After collecting the height and micromotion values over multiple frames, the average values are output to that trial’s data set and the code continues through each data point until the ion is ejected. Each trial is conducted at 20 fps with a subset of 15 frames analyzed for each DC voltage value.

To find the RF null point given a discrete data set, we selected the lowest 12 micromotion points in the data and fit them to a second-degree polynomial. The minimum of the micromotion versus voltage parabola was identified to be the RF null point. We then

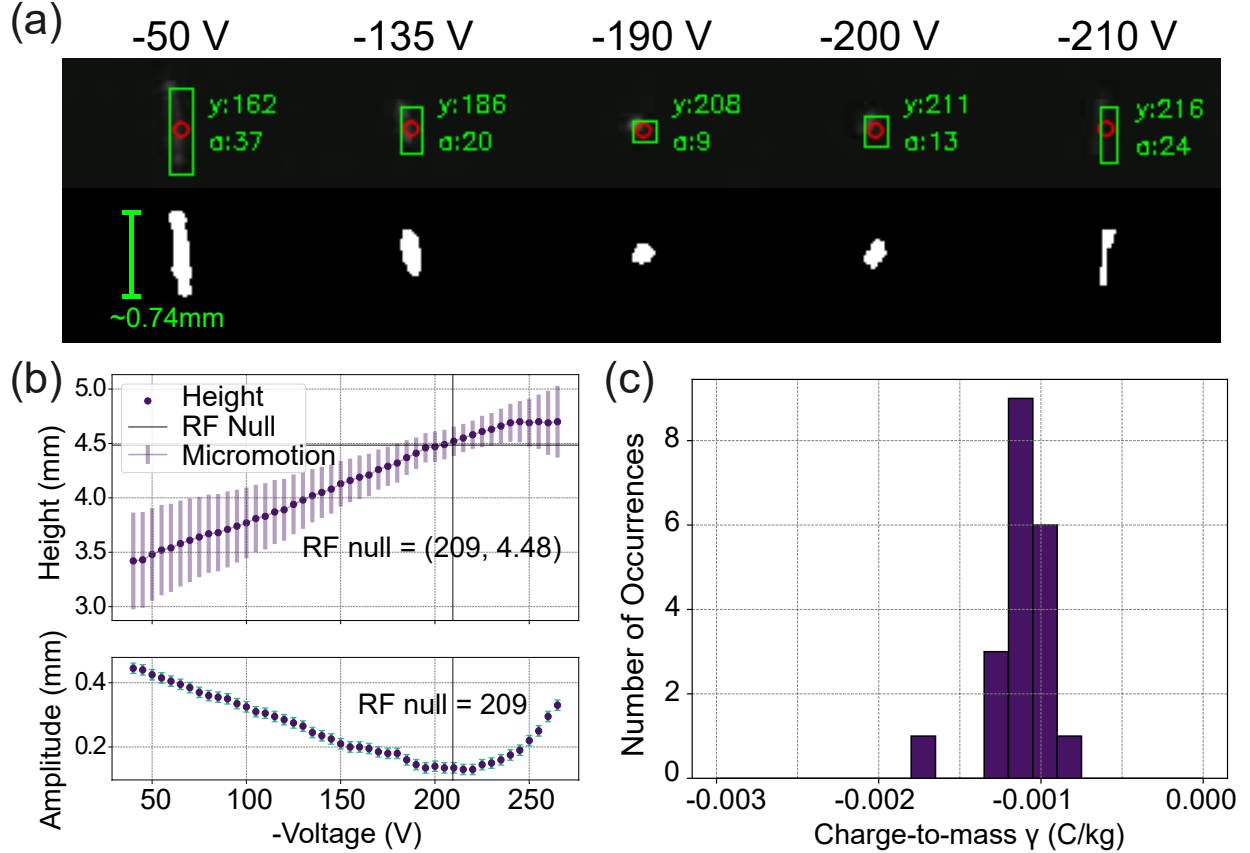


FIG. 3: Panel (a) shows the detected ion at different central electrode voltages with the location and amplitude of the ion labeled in units of pixels. On the bottom of panel (a) is the binarization after blob detection that is used for determining ion height and micromotion amplitude. The top axis of panel (b) shows the height of the ion versus the DC electrode voltage with the micromotion amplitude indicated by the light purple bars. The micromotion amplitude versus voltage is shown on the bottom axis with the measurement error corresponding to the size of a single pixel from the video ( $\sim 0.0164$  mm). The RF null point is indicated on both graphs as calculated above. Panel (c) is a histogram of the calculated charge-to-mass ratios ( $\gamma$ ) of an ensemble of 20 different trapped particles.

used a linear best fit of the voltage versus height data to find the intersection with our RF null central electrode voltage giving the height at the RF null. These two quantities, the applied central electrode voltage and the height at the RF null, enabled the calculation of the charge-to-mass ratio of the ions as detailed above in methods 1 and 2 and are compared in Fig. 4a.

**Results and Discussion:** We took several height versus central electrode voltage points for a given ion and compared methods 1 and 2 in Fig. 4a. The measured ion height versus DC voltage agrees better with the prediction of the model when  $\gamma$  is determined by method 1.

The offset when using method 2 can be explained by forces from the endcap electrodes that are not considered in the model, or stray potentials from the insulating cover of the enclosure. Analytic model agreement diverges at large negative DC electrode voltages when the particle begins to fall out of the trap. As shown in Fig. 4b At a certain threshold voltage, dependent on the charge-to-mass ratio, the trap becomes anti-confining the x-direction. However, we observe that the measured escape voltages typically exceed those predicted by the model by 10-20%, as seen in Fig. 4. Over 20 independent trials, the average voltage required to push a particle to the RF null was  $-185.3$  V, and the average measured voltage for escape was just above  $-225.5$  V. This discrepancy could be due to additional confinement in the x-direction from the endcap electrodes or to relatively slow dynamics of escape from the trap near the threshold.

Furthermore, we measured  $\gamma$  for the ions in those 20 trails using method 2 as shown in Fig. 3d. The mean  $\gamma$  of the ion ensemble was  $-1.13 \times 10^{-3}$  C/kg with a median of  $-1.07 \times 10^{-3}$  C/kg and a standard deviation of  $1.91 \times 10^{-4}$  C/kg. This data agrees with other measurements of charged lycopodium particles, which range from  $-2 \times 10^{-4}$  C/kg to  $-5 \times 10^{-2}$  C/kg<sup>10,12</sup>. The process of isolating one ion via filtration inherently selects higher charge-to-mass ratio particles, which can explain why the mean charge-to-mass ratio is large. The median RF null height was calculated to be  $4.38 \pm 0.295$  mm above the surface of the trap. These measurements agree with the analytic model's calculation of 4.56 mm with the voltage interpolation in the dielectric gaps.<sup>21</sup> A single camera pixel is  $\sim 0.0164$  mm and so the variation in measured values is not dominated by spatial measurement precision, but rather by some aspect of the trap or process of measurement. One possible explanation is stray fields due to the lack of control of the charge on the insulating enclosure.

## B. Ion Shuttling and Splitting

The primary appeal of QCCDs is dynamical positional control over trapped ions via segmented DC electrodes. Our apparatus allows for students to explore the dynamics of ion shuttling and splitting in these devices.

**Experimental Methods:** For these experiments we use a 6 mm focal length lens to image the ions and calibrate the length scale by imaging a fine ruler horizontally above the central DC electrode. For both the shuttling and splitting experiments, the power supply for the

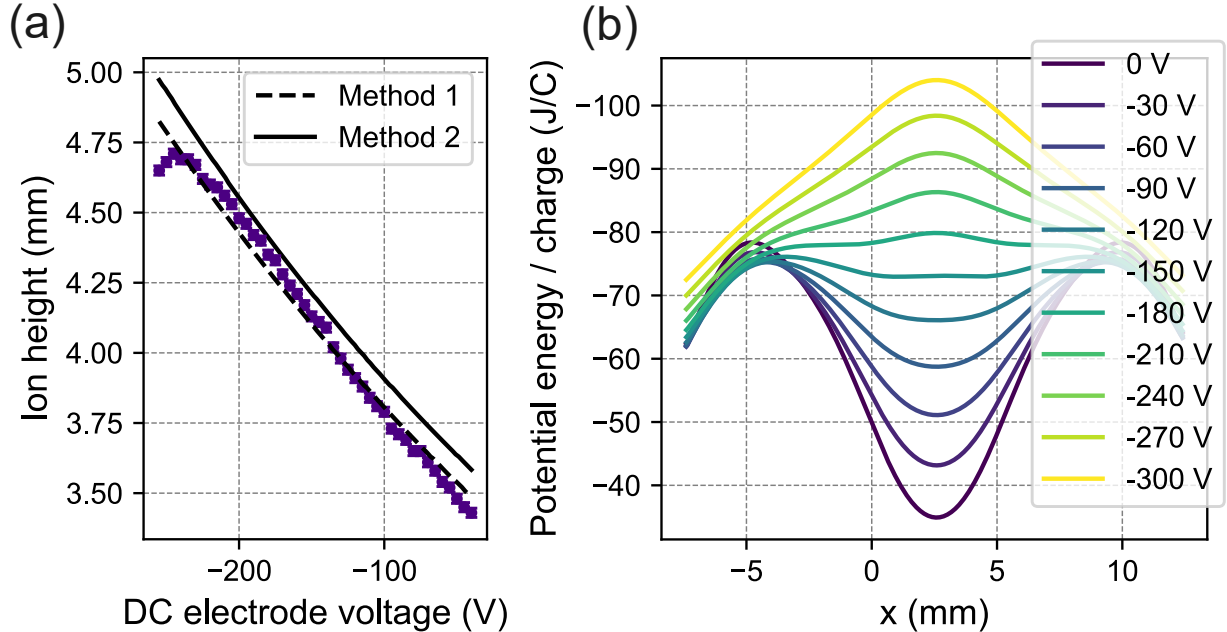


FIG. 4: Panel (a) shows ion height as a function of applied central DC voltage of one specific ion. Methods 1 and 2 for determining the charge-to-mass ratio are applied to this dataset, producing gamma values of  $\gamma_1 = -9.93 \times 10^{-4}$  C/kg and  $\gamma_2 = (-1.08 \pm 0.001) \times 10^{-3}$  C/kg respectfully. Panel (b) shows the potential along the  $x$ -axis at various applied central DC voltages with an example ion of charge-to-mass ratio  $\gamma_{\text{ex}} = -1.08 \times 10^{-3}$  C/kg .

AC electrodes is set to 50 V which is stepped up to around 1250 V. The power supply for the shuttling DC electrodes is set to  $-600$  V which was voltage-divided into the off, low, and high voltage settings via the relay circuit show in Fig. 1. The end caps are supplied with  $-225$  V and the central DC electrode is grounded.

To start each experiment, we load the trap with an ensemble of ions as in the previous section. The ions are initialized to center the particles in-line with the  $C$  DC electrode pair with a voltage pattern of high on electrodes  $A$  and  $E$ , low on electrodes  $B$  and  $D$ , and off on electrode  $C$ .

Once all of the ions are centered, we filter out those with lower charge-to-mass ratios just as in the previous section until only one or two particles remain in the trapping region, for demonstrating shuttling and splitting respectively. In both experiments, we switch the voltage configuration of the segmented electrodes and observe the resulting ion motion. For shuttling, the initial potential pattern is switched to a final pattern of “d center” with a voltage pattern of high on electrodes  $A$  and  $B$ , low on electrodes  $C$  and  $E$ , off on electrode

$D$ , and  $-226$  V on the  $END$  electrodes. For splitting, the same initial potential pattern is switched to a final pattern of “c split” in two stages. First, all of the segmented DC electrodes are set to “off” for approximately 1.5 seconds. Next, electrode  $C$  is set to “high”, electrodes  $A$  and  $E$  is set to “low”, and electrodes  $B$  and  $D$  are set to “off” to create a double-well potential, as shown in Fig.5b. Each shuttling and splitting video is analysed with OpenCV’s blob detection, where we assign each ion a tracking number to log their positions in each frame.

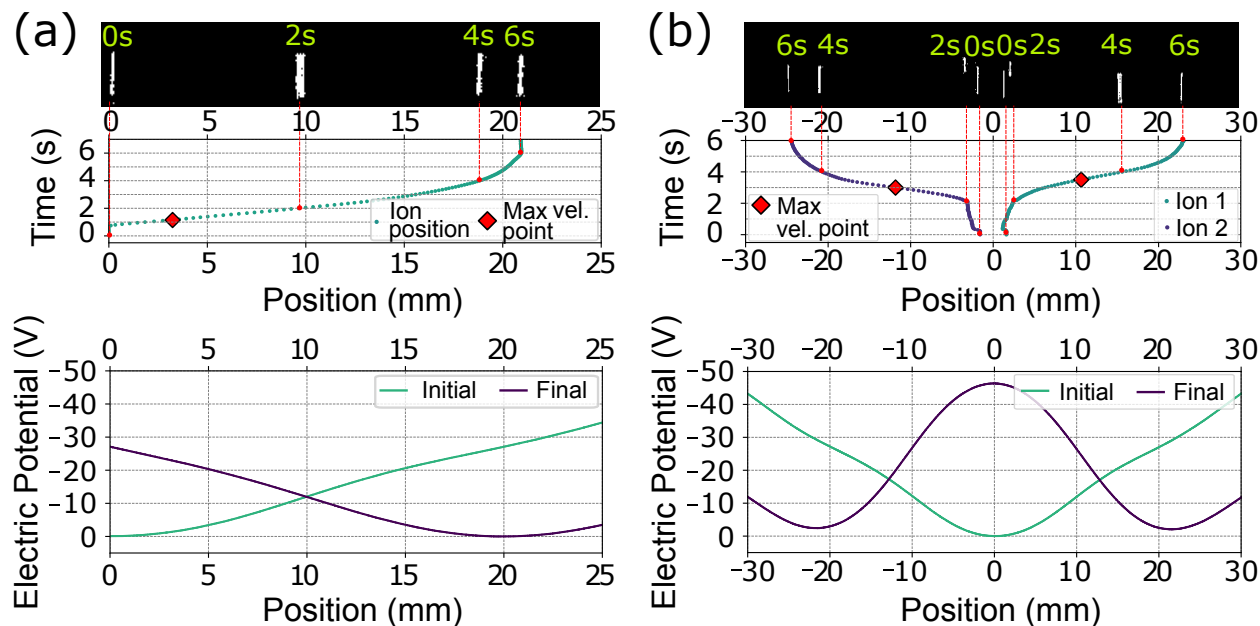


FIG. 5: Panel (a) shows ion shuttling and panel (b) shows ion splitting. In both panels, the top images show snapshots of ion positions in the trap as seen by our tracking program. These images correspond to the the middle plots of horizontal ion positions over time where their points of maximum velocity are marked with a red diamond. The initial and final ion positions are controlled by the locations of the initial and final potential pattern minima. The bottom graphs show each experiment’s corresponding COMSOL simulations of the potential from the segmented electrodes at the height of the analytic model’s predicted RF null. The green potential lines in these potential plots represent the initial potential while the dark purple lines represent the final potential. For shuttling, the initial potential forms a minimum at around position 0 mm and the final potential forms a minimum at 21 mm. The same goes for splitting with the addition of another final potential minimum at  $-21$  mm. Note that the position axis here corresponds to the  $z$ -axis of figure 1.

**Results and Discussion:** In Fig. 5 panel (a), we can see that the ion quickly accelerates to its maximum velocity of approximately  $10.0$  mm/s before settling in the new potential well. This agrees with the bottom plot which shows a COMSOL simulation of the potential

patterns created by the DC electrode pairs to shuttle our ion. The point of maximum velocity occurs soon after the switch to high potential on the left while the slowing of the ion occurs as it enters its new potential well after 20 mm.

In Fig. 5 panel (b), we can see similar shuttling behavior in each of the splitting ions. They reached their maximum velocities of about  $-15.3$  mm/s and  $11.8$  mm/s early in their individual motion before they slowed into their respective potential wells. However, the main difference is that at the very beginning of their motion, when the electrode pattern was set to “all off,” the ions were allowed to push apart from each other for about 1.5 seconds before we drove a potential peak between them with a high voltage applied to the  $C$  DC electrode pair. Applying potential patterns in this way led to more consistent splitting between the ions because their mutual coulomb repulsion frequently positioned them on opposite sides of the following central peak.

## V. EXTENSIONS TO THE SETUP

We have a number of additional exercises with the described setup that we intend to offer as open-ended final projects in the next iteration of the course. One follow-up design exercise is to imagine how the design must be modified to trap  $\text{Ca}^+$  ions where the charge-to-mass ratio is  $2.4\text{E}6$  C/kg<sup>17,21,23</sup>. Electrical engineers could identify design solutions to produce the needed voltages and frequencies for optimal trapping and shuttling performance. Another simple hands-on exercise is to measure the micromotion frequency of the trapped ions, which should be at the AC driving frequency, by either strobing the illumination laser at different frequencies or sweeping the camera frame rates, both using the stroboscopic effect.<sup>11</sup> Students could also determine the damping coefficient of air based on the damped dynamics of the shuttling particles<sup>25</sup> by fitting the ion trajectory data to a mechanical model with damping, either extending the analytic model of the trap to include the segmented electrodes or using the COMSOL model from Fig. 5. The transition between 1D and 2D Coulomb crystals is another property students could explore with adequately large segmented electrode voltages.<sup>11</sup>

There are several physical modifications and extensions to the setup which could be implemented to improve or expand the capabilities of the lab. The addition of a grounded plate above the trap would increase trap depth and improve control over fields from stray

charges.<sup>25</sup> Distinct ion-chain secular mode excitation may be possible on this setup with the usage of electrospray ionization with glycerin.<sup>16</sup> We have been unable to observe clearly resolved secular modes with the lycopodium moss spores, most likely because these modes are in the overdamped regime.<sup>10,14</sup> Another improvement would be to try to apply analog signals to the shuttling electrodes via a digital-to-analog converter. This would allow for smoother shuttling, the exploration of different shuttling waveforms and their impact on shuttling and splitting.<sup>24</sup> The setup could be taken to the next level of relevance to current research by redesigning it to implement “X” and “T” junctions, which are important in QCCDs.<sup>26</sup> More exotic RF trap geometries, such as 2D arrays<sup>27</sup> or 3D multilevel traps<sup>24</sup> would also be interesting to explore in a macroscopic regime.

## VI. ACKNOWLEDGEMENTS

We thank Enrique Garcia and Jaidon Lybbert for their invaluable guidance with the relay circuit design. We thank Dr. Alejandro Garcia for loaning us a high-voltage power supply early in the project. We thank Carl Thomas, Jane Gunnell, and Dr. Alexander Kato for their assistance at the start of the project, and Dr. Sara Mouradian for her suggestions on determining the necessary shuttling voltages and feedback on the manuscript. This work was supported by the National Science Foundation under awards DMR-2019444 (IMOD an NSF-STC) and PHY-2011503, and by the University of Washington Student Technology Fee. This project is part of the Quantum Technologies Training and Testbed (QT3) laboratory at the University of Washington, which is supported by NIST award 60NANB23D202.

## APPENDIX: ANALYTIC MODEL FREE-SPACE POTENTIAL FUNCTIONS

If one assumes the traits listed in section III for the trap geometry, one can use an analytic model to produce specific functions for  $\phi_{\text{RF}}(\mathbf{r})$  and  $\phi_{\text{DC}}(\mathbf{r})$ . Let the origin of our coordinate system be at the bottom left-most corner of the central electrode. Now, assume that the widths of the central and RF electrodes extend to infinity, which is a good approximation if the RF null axis has a height above the central electrode that is small relative to the width of the electrodes. Also, assume that each electrode extends its edges to the middle of each dielectric gap. Then, an electrode of edges at locations  $x_1$  and  $x_2$  relative to the origin has



an in-plane voltage distribution of

$$\phi_i(x, y = 0) = \begin{cases} V_i, & x \in (x_1, x_2) \\ 0, & \text{else} \end{cases}$$

which produces a corresponding free-space voltage above the plane of  $\phi_i(x, y > 0) =$

$$\frac{V_i}{\pi} \left[ \arctan\left(\frac{x_2 - x}{y}\right) - \arctan\left(\frac{x_1 - x}{y}\right) \right] \quad (5)$$

where the potential is independent of the z-coordinate due to the translational symmetry of the infinite electrode length assumption.<sup>21</sup> Therefore, a central electrode of sides  $x_1 = 0, x_2 = a$  has an in-plane voltage of

$$\phi_{\text{DC}}(x, y = 0) = \begin{cases} V_{\text{DC}}, & x \in (0, a) \\ 0, & \text{else} \end{cases}$$

with corresponding free-space voltage of  $\phi_{\text{DC}}(x, y > 0) =$

$$\frac{V_{\text{DC}}}{\pi} \left[ \arctan\left(\frac{a - x}{y}\right) + \arctan\left(\frac{x}{y}\right) \right] \quad (6)$$

and RF electrodes with

$$\phi_{\text{RF}}(x, y = 0, t) = \begin{cases} V_{\text{RF}} \cos \Omega t, & x \in (-c, 0) \cup (a, a + b) \\ 0, & \text{else} \end{cases}$$

produce free space voltages of  $\Phi_{\text{RF}}(x, y > 0, t) =$

$$\begin{aligned} & \frac{V_{\text{RF}}}{\pi} \left[ \arctan\left(\frac{a + b - x}{y}\right) + \arctan\left(\frac{c + x}{y}\right) \right. \\ & \left. - \left( \arctan\left(\frac{a - x}{y}\right) + \arctan\left(\frac{x}{y}\right) \right) \right] \cos \Omega t \\ \implies & \Phi_{\text{RF}}(x, y > 0, t) = \phi_{\text{RF}}(x, y > 0) \cos(\Omega t) \end{aligned} \quad (7)$$

where  $\phi_{\text{RF}}(x, y > 0)$  is the separable, time independent part of  $\Phi_{\text{RF}}(x, y > 0, t)$ . Therefore, we can combine equations 6 and 7 get a solution for  $\frac{\mathcal{U}}{q}$ .

One can determine  $\frac{\mathcal{U}}{q}$  without the infinite electrode assumption by using the analytic function for a finite electrode described by House in addition to simulating other finite electrodes in the model such as the endcap electrodes.<sup>21,28</sup> However, calculating  $|\nabla\phi_{\text{RF}}(\mathbf{r})|^2$  becomes significantly more difficult.

## BILL OF MATERIALS

**Total Apparatus Price: \$7,143.17 (USD as of 10/14/2024)**

TABLE I: Primary Components and Breadboard Peripherals

Item	Application	Supplier	Part Number	Price/Item	Qty.	Price
<b>Primary Components</b>						
Variac	AC Voltage Supply	Amazon	B07Y4ZY3K1	\$57.17	1	\$57.17
Transformer <sup>a</sup>	Step-up AC Voltage	Static Clean	F-90117	\$437.00	1	\$437.00
HV Cable <sup>a</sup>	Transformer Peripheral	Static Clean	F-80312	\$11.00	1	\$11.00
HP Connector Kit <sup>a</sup>	Transformer Peripheral	Static Clean	F-90100	\$20.00	1	\$20.00
HV-DC Supply	DC Voltage Supply	SRS <sup>b</sup>	PS310	\$2,650.00	1	\$2,650.00
HV-DC Supply	Endcap Voltage Supply	Digikey	1470-3186-ND	\$138.81	1	\$138.81
Function Generator	Produce END Voltage	Siglent	SDG1032X	\$359.00	1	\$359.00
Arduino Mega	Control of Reed Relays	arduino.cc	A000067	\$53.00	1	\$53.00
Blackfly S Camera	Imaging	Edmund Optics	22-078	\$655.00	1	\$655.00
1 mW Laser	Illumination	Edmund Optics	37-029	\$123.00	1	\$123.00
PLA (1.75 mm, Black)	Structural Support	Amazon	B07PGY2JP1	\$23.99	3	\$71.97
Acrylic	Optical Ports	Amazon	B07RY4X9L3	\$16.95	1	\$16.95
Breadboard	Fastening Components	Thorlabs	MB1218U	\$216.05	1	\$216.05
6 mm Lens	Shuttling Lens	Edmund Optics	33-301	\$260.00	1	\$260.00
25 mm Lens	Micromotion Lens	Edmund Optics	59-871	\$325.00	1	\$325.00
Wool	Particle Charging	Amazon	B07D6XG3S4	\$9.89	1	\$9.89
Lycopodium Moss Spores	Working Ions	SKS <sup>c</sup>	LYCOP2	\$69.00	1	\$69.00
Teflon Rod	Particle Charging	Amazon	B01BSLI1YG	\$12.03	1	\$12.03
Cat 5e GigE Cable	Camera Signal	Edmund Optics	86-785	\$62.00	1	\$62.00
<b>Breadboard Peripherals</b>						
Laser Diode Mount	Fasten Laser	Edmund Optics	37-144	\$90.00	1	\$90.00
Camera Mount	Fasten Camera	Edmund Optics	15-838	\$37.50	1	\$37.50
Switch	Toggle Laser	Digikey	360-1887-ND	\$6.70	1	\$6.70
Laser Power Supply	Power Laser	Edmund Optics	59-099	\$66.50	1	\$66.50
Metal Screws and Bolts	Fastening Breadboard Items	Thorlabs	HW-KIT2	\$139.58	1	\$139.58
Post Clamps	Fastening Laser and Camera	Thorlabs	CF125	\$9.68	2	\$19.36
Post Holders	Fasten Posts to Breadboard	Thorlabs	PH1.5E	\$27.92	2	\$55.84
1.5" Posts	To hold Camera and Laser	Thorlabs	TR1.5	\$5.65	2	\$11.30
Nylon Screw (6-40)	Fasten Trap to Enclosure	McMaster	95868A908	\$13.79	1	\$13.79
Nylon Screw (1/4-20)	Fasten Relay Circuit	McMaster	95868A744	\$15.78	1	\$15.78
Nylon Nut (1/4-20)	Fasten Relay Circuit	McMaster	94812A700	\$13.24	1	\$13.24
Nylon Nut (6-40)	Fasten Trap to Enclosure	McMasteer	94812A663	\$12.95	1	\$12.95
<b>Total Table Price:</b>						<b>\$6,029.41</b>

<sup>a</sup> Transformer and other peripherals listed where not used in our experiments and have not been tested.

Any 60 Hz transformer which steps up  $\sim 120$  V to  $\sim 6$  kV should work for the apparatus

<sup>b</sup> Stanford Research Systems

<sup>c</sup> <sciencekitstore.com>

TABLE II: Circuit Parts

Item	Application	Supplier	Part Number	Price/Item	Qty.	Price
<b>Miscellaneous Parts</b>						
Ring Terminals	Attach Wires to Board	McMaster	7113K552	\$18.68	1	\$18.68
SHV Cable	Attach HV-DC to Circuit	Digikey	3985-PE33018-12-ND	\$109.99	1	\$109.99
HV Wire (10 ft)	Connect Components	McMaster	8296K11	\$54.80	1	\$54.80
SHV Terminal	Attach HV-DC to Circuit	Digikey	A24669-ND	\$26.33	2	\$52.66
5 V DC	Power Relay Circuit	Amazon	B09NLMVXMZ	\$7.98	1	\$7.98
Banana Plug M (W)	Wires to Banana Plugs	Digikey	J144-ND	\$2.65	2	\$5.30
Banana Plug M (R)	Wires to Banana Plugs	Digikey	J145-ND	\$2.74	2	\$5.48
Banana Plug M (G)	Wires to Banana Plugs	Digikey	J340-ND	\$2.83	2	\$5.66
Banana Plug M (BK)	Wires to Banana Plugs	Digikey	J146-ND	\$2.71	2	\$5.42
Banana Plug M (B)	Wires to Banana Plugs	Digikey	J344-ND	\$1.52	2	\$3.04
Banana Plug M (O)	Wires to Banana Plugs	Digikey	J341-ND	\$2.58	2	\$5.16
Banana Plug M (GY)	Wires to Banana Plugs	Digikey	J346-ND	\$2.29	2	\$4.58
Banana Plug M (PL)	Wires to Banana Plugs	Digikey	J345-ND	\$2.33	2	\$4.66
Banana Plug M (Y)	Wires to Banana Plugs	Digikey	J342-ND	\$2.72	2	\$5.44
Banana Plug F (W)	Wires to Banana Plugs	Digikey	J150-ND	\$1.38	2	\$2.76
Banana Plug F (R)	Wires to Banana Plugs	Digikey	J151-ND	\$1.31	2	\$2.62
Banana Plug F (G)	Wires to Banana Plugs	Digikey	J153-ND	\$1.45	2	\$2.90
Banana Plug F (BK)	Wires to Banana Plugs	Digikey	J118-ND	\$1.31	2	\$2.62
Banana Plug F (B)	Wires to Banana Plugs	Digikey	J155-ND	\$1.44	2	\$2.88
Banana Plug F (O)	Wires to Banana Plugs	Digikey	J356-ND	\$1.20	2	\$2.40
Banana Plug F (GY)	Wires to Banana Plugs	Digikey	J359-ND	\$1.28	2	\$2.56
Banana Plug F (PL)	Wires to Banana Plugs	Digikey	J358-ND	\$1.33	2	\$2.66
Banana Plug F (Y)	Wires to Banana Plugs	Digikey	J154-ND	\$1.11	2	\$2.22
10 M Resistors	Current Limiter	Digikey	4506-HVLR3908F10MOK9-ND	\$14.03	2	\$28.06
1 M Resistors	Current Limiter	Digikey	VR68J1.0MCT-ND	\$0.93	2	\$1.86
HV Tape	Apply on Solder Joints	McMaster	7682A42	\$31.07	1	\$31.07
Shrink Tubing Kit	Cover Solder Joints	Digikey	298-11579-ND	\$99.25	1	\$99.25
<b>Planar Electrode Circuit</b>						
Test Point	Use to Probe Electrodes	Digikey	36-5199CT-ND	\$0.33	1	\$0.33
Black Terminal	Wires to Electrodes	Digikey	1849-1168-1-ND	\$1.26	3	\$3.78
Red Terminal	Wires to Electrodes	Digikey	1849-1170-1-ND	\$1.26	1	\$1.26
Blue Terminal	Wires to Electrodes	Digikey	1849-1156-1-ND	\$1.26	1	\$1.26
Green Terminal	Wires to Electrodes	Digikey	1849-1155-1-ND	\$1.26	1	\$1.26
White Terminal	Wires to electrodes	Digikey	1849-1171-1-ND	\$1.26	1	\$1.26
Yellow Terminal	Wires to Electrodes	Digikey	1849-1169-1-ND	\$1.26	1	\$1.26
Planar Trap Board PCB	Ion Trapping	OSH Park	N.A.	\$77.30	1	\$77.30
SHV to BNC Adapter	Ground SHV	ThorLabs	T4004	\$50.5	1	\$50.50
BNC Terminator	Ground SHV	L-com	BM50G-1W	\$11.59	2	\$23.18
<b>Relay Circuit</b>						
Relay Circuit PCB	Give Structure to Circuit	Osh Park	N.A.	\$285.00	1	\$285.00
PCB Stencil	Help with Soldering	Osh Stencils	N.A.	\$29.09	1	\$29.09
Solder Paste	Solder SMD Components	Digikey	315-NC191LT10-ND	\$7.95	1	\$7.95
Reed Relays	Shuttling Voltages	Digikey	306-1193-ND	\$12.05	10	\$120.50
Terminal Block (7)	Output Interface	Digikey	A135925-ND	\$4.48	1	\$4.48
Terminal Block (3)	Input Interface	Digikey	A98085-ND	\$1.70	1	\$1.70
1 M Resistor	N.A.	Digikey	A138410CT-ND	\$0.22	16	\$3.57
100 M Resistor	N.A.	Digikey	A105971CT-ND	\$0.43	6	\$2.58
Diodes	Flyback Diodes for Relays	Digikey	ZLLS410CT-ND	\$0.37	10	\$3.67
5 V Jack	Power MOSFETS	Digikey	2073-DCJ250-05-A-K1-ACT-ND	\$1.02	1	\$1.02
300 $\Omega$ Resistor	N.A.	Digikey	A121216CT-ND	\$0.90	10	\$9.01
3.3 k Resistor	N.A.	Digikey	408-1639-1-ND	\$2.73	10	\$27.26
MOSFET	Switch Reed Relays	Digikey	NTA7002NT1GOSCT-ND	\$0.16	10	\$1.61
Signal Terminal (12)	Signal Transfer	Digikey	2057-SMC-1-12-1-GT-ND	\$0.90	1	\$0.90
<b>Total Table Price:</b>						<b>\$1,113.76</b>

---

\* mfpars@uw.edu

- <sup>1</sup> Subcommittee on Quantum Information Science, “Quantum Information Science and Technology Workforce Development National Strategic Plan,” (2022)
- <sup>2</sup> Oliver Ezratty, *Understanding Quantum Technologies*, 6th Ed. (Creative Commons), 448-473 (2023)
- <sup>3</sup> Sukhpal S. Gill, Adarsh Kumar *et al*, “Quantum computing: A taxonomy, systematic review and future directions,” *Software: Practice and Experience* **52(1)**, 66-114 (2022)
- <sup>4</sup> Colin D. Bruzewicz, John Chiaverini, Robert McConnell, and Jeremy M. Sage, “Trapped-Ion Quantum Computing: Progress and Challenges,” *Applied Physics Reviews*, 021314 (2019)
- <sup>5</sup> Francesco Bernardini, Abhijit Chakraborty, and Carlos Ordóñez, “Quantum computing with trapped ions: a beginner’s guide,” *Eur. J. Phys.* **45**, 013001 (2023)
- <sup>6</sup> V. Kaushal, B. Lekitsch, A. Stahl, J. Hilder, D. Pijn, C. Schmiegelow, A. Bermudez, M. Müller, F. Schmidt-Kaler, U. Poschinger, “Shuttling-Based Trapped-Ion Quantum Information Processing,” *AVS Quantum Sci.* **1 2 (1)**, 014101 (2020).
- <sup>7</sup> S. A. Moses, C. H. Baldwin, M. S. Allman *et al*, “A Race-Track Trapped-Ion Quantum Processor,” *Phys. Rev. X* **13**, 041052 (2023)
- <sup>8</sup> D. Kielpinski, C. Monroe, and D.J. Wineland, “Architecture for a large-scale ion-trap quantum computer,” *Nature* **417**, 709–711 (2002)
- <sup>9</sup> Cole E. Wolfram, Noah B. Warren, Robert E. Thomas, and Maxwell F. Parsons, computer code `Planar Trap Laboratory Data Analysis and Visualization`, <<https://github.com/qt3uw/qt3-ion-trap.git>>.
- <sup>10</sup> Edgar Perez and John Essick, “Chaos in the monopole ion trap,” *Am. J. Phys.* **89**, 84-95 (2021)
- <sup>11</sup> Kenneth G. Libbrecht and Eric D. Black, “Improved microparticle electrodynamic ion traps for physics teaching,” *Am. J. Phys.* **86**, 539–558 (2018)
- <sup>12</sup> M. A. Timmer, “Trapping Lycopodium Spores in a Vertical Linear Paul Trap,” Bachelor’s Thesis, University of Groningen, (2023).
- <sup>13</sup> N. Rey Whetten, “Macroscopic particle motion in quadrupole fields,” *Journal of Vacuum Science and Technology* **11**, 515–518 (1974)
- <sup>14</sup> H. Winter and H. W. Ortjohann, “Simple demonstration of storing macroscopic particles in a

- ‘Paul trap’,” *Am. J. Phys.* **59**, 807–813 (1991)
- <sup>15</sup> L M Vasilyak *et al*, “Coulomb stable structures of charged dust particles in a dynamical trap at atmospheric pressure in air,” *New J. Phys.* **15**, 043047 (2013)
- <sup>16</sup> Scott Robertson and Richard Younger, “Coulomb crystals of oil droplets,” *Am. J. Phys.* **67** (4), 310–315 (1999)
- <sup>17</sup> Seokjun Hong, Minjae Lee, Hongjin Cheon, Taehyun Kim, and Dong-il “Dan” Cho, “Guidelines for Designing Surface Ion Traps Using the Boundary Element Method,” *Sensors* **16**, 616-632 (2016)
- <sup>18</sup> Gebhard Littich, “Electrostatic Control and Transport of Ions on a Planar Trap for Quantum Information Processing,” Master’s Thesis, University of California, Berkeley, (2011).
- <sup>19</sup> Robert Tarzwell and Ken Bahl, *High Voltage Printed Circuit Design & Manufacturing Notebook*, SIERRA Proto Express, (2004)
- <sup>20</sup> OpenCV, “SimpleBlobDetector Class Reference,” <[https://docs.opencv.org/4.x/d0/d7a/classcv\\_1\\_1SimpleBlobDetector.html](https://docs.opencv.org/4.x/d0/d7a/classcv_1_1SimpleBlobDetector.html)>
- <sup>21</sup> M. G. House, “Analytic model for electrostatic fields in surface-electrode ion traps,” *Phys. Rev. A* **78**, 033402 (2008).
- <sup>22</sup> Altaf H. Nizamani and Winfried K. Hensinger, “Optimum electrode configurations for fast ion separation in microfabricated surface ion traps,” *Appl. Phys. B* **106**, 327–338 (2012)
- <sup>23</sup> Arkadas Ozakin and Fayaz Shaikh, “Stability analysis of surface ion traps,” *J. Appl. Phys.* **112**, 074904 (2012)
- <sup>24</sup> D. Hucul, M. Yeo, S. Olmschenk, and C. Monroe, “On the Transport of Atomic Ions in Linear and Multidimensional Ion Trap Arrays,” *Quantum Inf. Comput.* **8**, 501-578 (2008)
- <sup>25</sup> C. E. Pearson, “Theory and Application of Planar Ion Traps,” Master’s thesis, Massachusetts Institute of Technology, (2006).
- <sup>26</sup> J. Chiaverini, B. Blakestad, J. Britton, J.D. Jost, C. Langer, D. Leibfried, R. Ozeri, and D.J. Wineland, “Surface-Electrode Architecture for Ion-Trap Quantum Information Processing,” *Quantum Inf. Comput.* **5**, 419–439 (2005)
- <sup>27</sup> C. E. Pearson, D. R. Leibbrandt, W. S. Bakr, W. J. Mallard, K. R. Brown, and I. L. Chuang, “Experimental investigation of planar ion traps,” *Phys. Rev. A* **73**, 032307 (2006)
- <sup>28</sup> Zachary Fisher, “Shuttling of Ions for Characterization of a Microfabricated Ion Trap,” Bachelor’s thesis, Massachusetts Institute of Technology, (2012)